

## Article

# Preparing Co/N-Doped Carbon as Electrocatalyst toward Oxygen Reduction Reaction via the Ancient “Pharaoh’s Snakes” Reaction

Jian Gao <sup>1,2,\*</sup>, Mengxin Zhou <sup>1</sup>, Xinyao Wang <sup>1</sup>, Hong Wang <sup>1</sup>, Zhen Yin <sup>3</sup>, Xiaoyao Tan <sup>1,\*</sup> and Yuan Li <sup>1,\*</sup>

<sup>1</sup> Tianjin Key Laboratory of Green Chemical Engineering Process Engineering, Tiangong University, Tianjin 300387, China

<sup>2</sup> Haian Nanjing University High Tech Institute, 428, Zhennan Road, Haian 226600, China

<sup>3</sup> College of Chemical Engineering and Materials Science, Tianjin University of Science and Technology, 29 13th Avenue, TEDA, Tianjin 300457, China

\* Correspondence: gaojian@tiangong.edu.cn (J.G.); tanxiaoyao@tiangong.edu.cn (X.T.); liyuan@tiangong.edu.cn (Y.L.)

**Abstract:** The oxygen reduction reaction (ORR) is of great importance for clean energy storage and conversion techniques such as fuel cells and metal–air batteries (MABs). However, the ORR is kinetically sluggish, and expensive noble metal catalysts are required. The high price and limited preservation of noble metal catalysts has largely hindered the wide application of clean power sources such as fuel cells and MABs. Therefore, it is important to prepare non-expensive metal catalysts (NPMC) to cut the price of the fuel cells and MABs for wide application. Here, we report the preparation of a  $\text{Co}_3\text{O}_4$  carried on the N-doped carbon (Co/N-C) as the ORR NPMC with a facile Pharaoh’s Snakes reaction. The gas generated during the reaction is able to fabricate the porous structure of the resultant carbon doped with heteroatoms such as Co and N. The catalyst provides a high electrocatalytic activity towards ORR via the 4-e pathway with an onset and half-wave potential of 0.98 and 0.79 V (vs. RHE), respectively, in an electrolyte of 0.1 M KOH. The onset and half-wave potentials are close to those of the commercial Pt/C. This work demonstrates the promising potential of an ancient technology for preparing NPMCs toward the ORR.

**Keywords:** oxygen reduction reaction; non-precious metal catalyst; Pharaoh’s snakes; electrocatalysts; Li-air battery



**Citation:** Gao, J.; Zhou, M.; Wang, X.; Wang, H.; Yin, Z.; Tan, X.; Li, Y. Preparing Co/N-Doped Carbon as Electrocatalyst toward Oxygen Reduction Reaction via the Ancient “Pharaoh’s Snakes” Reaction. *Batteries* **2022**, *8*, 150. <https://doi.org/10.3390/batteries8100150>

Academic Editor: Wenbo Liu

Received: 18 July 2022

Accepted: 26 September 2022

Published: 1 October 2022

**Publisher’s Note:** MDPI stays neutral with regard to jurisdictional claims in published maps and institutional affiliations.



**Copyright:** © 2022 by the authors. Licensee MDPI, Basel, Switzerland. This article is an open access article distributed under the terms and conditions of the Creative Commons Attribution (CC BY) license (<https://creativecommons.org/licenses/by/4.0/>).

## 1. Introduction

The rapid depletion of fossil fuels and severe ecological deterioration have made it urgent to develop sustainable and clean energy sources to address the issues regarding energy and environmental [1]. Due to their environmental friendliness and high energy density, fuel cells and metal–air batteries (MABs, such as the Zn-Air and Li-Air batteries) are considered to be excellent candidates for various applications such as stationary power generation, mobile power source, and transportation in the future [2,3]. In fuel cells and MABs, the chemical energy in the fuels is transformed directly into electric power free of the Carnot recycle. Therefore, the fuel cells and MABs possess efficiencies higher than those of tradition technologies that generate electric power based on combustion.

Despite these encouraging advantages, fuel cells and MABs still face several challenges. One of the challenges is their high price because of their dependence on noble metal catalysts. In both fuel cells and MABs, the  $\text{O}_2$  or the  $\text{O}_2$  in the air is reduced via the oxygen reduction reaction (ORR) on the cathode during discharge [4–6]. According to the ORR mechanism model proposed by Wroblowa et al. in 1976 [7], the ORR takes place by means of a complicated process, resulting in the sluggishness of the ORR. The sluggish ORR necessitates the use of the corresponding catalysts [8]. The state-of-the-art catalysts for the

ORR are mostly platinum-based materials. However, the high cost of platinum has thus far prohibited the wide use of the catalyst and, consequently, the corresponding energy conversion and storage devices. Apart from the high price, the limited preserve of Pt is also a significant challenge that has also severely impeded the wide application of Pt catalysts and new energy systems such as fuel cells and MABs. One approach to solving this problem is to reduce the usage of Pt catalysts by improving the Pt use efficiency in the catalyst layers. The use efficiency can be improved by alloying Pt with non-precious metals such as Fe, Co, Ni, etc., or by supporting the catalyst on carrier materials. However, the reduction in Pt loading has been totally offset by increasing Pt prices, rendering efforts devoted to reducing Pt loading in the last two decades almost totally ineffective [9]. Therefore, Pt loading reduction seems not to be a long-term solution for reducing the cost of catalysts for fuel cells or MABs. Another promising approach is to develop non-precious-metal electrocatalysts (NPMCs) from non-Pt metals (non-PGM) [9,10]. Since no precious metals are needed in the catalyst, this approach is an ideal strategy in the long run, making possible the wide application of clean and efficient storage and conversion devices such as the fuel cell and MABs [9,11].

In recent years, transition metals carried on heteroatom-doped carbon (M/N-C) materials have been widely investigated as NPMCs for ORR [9]. In this field, great efforts have been devoted to developing methods for preparing the NPMCs [9,12]. Generally, materials rich in porous structures are more likely to provide high catalytic activity. A tremendous amount of work has been conducted on the preparation of porous catalysts for ORR. Some examples of this are as follows: aerogels were heated to prepare porous catalysts for ORR with an onset potential of 0.92 V vs. RHE ( $V_{RHE}$ ) [13]. Metal–organic frameworks (MOFs) were investigated as self-sacrificing precursors or templates for the preparation of nano-porous carbons [14]. Hard templates and  $NH_3$  were used to prepare porous ORR catalysts [15], and an onset potential of  $\sim 1$  V<sub>RHE</sub> was obtained. While trying to prepare efficient porous catalysts, some scientists have been inspired by ancient knowledge, and encouraging results have been achieved [12,16,17]. The “Pharaoh’s snakes” reaction is a famous reaction for generating foam materials. In this reaction, great amounts of gases are generated, resulting in the fabrication of a porous, foam-like product. Therefore, this “Pharaoh’s snakes” reaction holds great promise for providing an ORR catalyst with high activity. With sugar, melamine and iron nitrate as precursors, Fe/N-C has been prepared using the “Pharaoh’s snakes” reaction that exhibited high performance [12]. However, the Fe ions dissolved from Fe/N-C were detrimental to battery durability. The Fe ions catalyze radical formation from  $H_2O_2$  via Fenton reactions [8]. These radicals degrade battery components such as organic ionomers, membranes and the Fe/N-C catalyst itself [18]. Therefore, it is necessary to replace Fe with metals that do not catalyze Fenton reactions [19], and Co is such a promising alternative choice [20]. However, the preparation of Co/N-C catalysts using the “Pharaoh’s snakes” reaction has rarely been performed.

In this study, porous Co/N-C was prepared using a slightly adjusted “Pharaoh’s snakes” method, and was investigated as a catalyst for ORR in alkaline electrolyte. The master catalyst sample shows an onset and a half-wave potential of 0.98 and 0.79 V<sub>RHE</sub>, respectively. These results demonstrate an interesting application of an ancient reaction to solve a modern problem.

## 2. Experimental Section

### 2.1. Preparation of Electrocatalysts

As displayed in Figure 1, sugar powder (3 g),  $NH_4HCO_3$  (0.8 g), melamine (2.4 g),  $Co(NO_3)_2 \cdot 6H_2O$  (0.1 g) were mixed with purified water to prepare a solution, which was then dried, ground in a mortar, and burned to obtain a snake-like foam ash. The ash was then pyrolyzed in a tubular furnace with a nitrogen stream of  $60\text{ mL min}^{-1}$  at  $900\text{ }^\circ C$  for 1 h with a rate of temperature increase of  $5\text{ }^\circ C\text{ min}^{-1}$ . A black carbon material (Co/N-C-900) was obtained when the furnace was cooled to room temperature. The temperature–time curve is presented in Figure S1 in the Supplementary Materials (ESI). The Co/N-C was also

prepared with pyrolyzing temperatures of 800 (Co/N-C-800) and 1000 °C (Co/N-C-1000) to investigate the influence of the pyrolyzing temperature on catalytic activity.

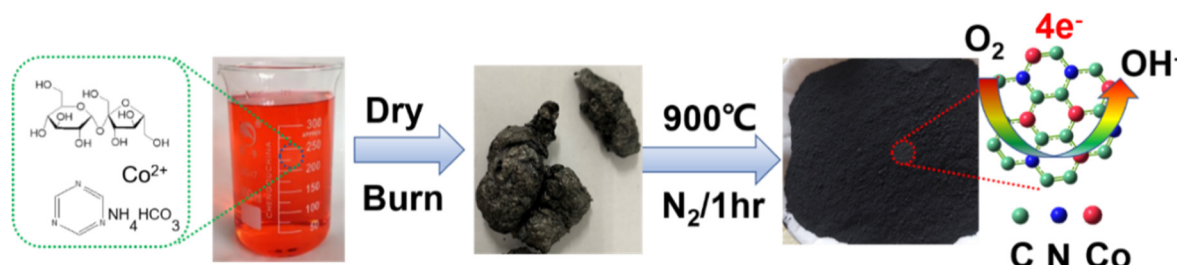


**Figure 1.** A schematic illustration of the preparation of the Co/N-C using the “Pharaoh’s snakes” reaction.

## 2.2. Characterization

The catalyst morphologies were examined using a scanning electron microscope (FESEM, JEOL JSM-7500F) and a field emission transmission electron microscope (TEM, JEOL JEM-2100F). X-ray diffraction (XRD) patterns were collected with Cu K $\alpha$  radiation ( $\lambda = 1.5406 \text{ \AA}$ ) (Panalytical, Empyrean). A confocal micro-Raman spectrometer (Jobin Yvon Laboratory RAM HR1800) was used to determine the Raman spectra through a 10 $\times$  microscope objective with backscattered geometry. An Ar $+$  laser was used as an excitation source, emitting at a wavelength of 633 nm.

The specific surface area and pore size were measured using nitrogen adsorption/desorption isotherms (Micromeritics ASAP 2020 V3.00 H) by means of the Brunauer–Emmett–Teller (BET) and Barrett–Joyner–Halenda (BJH) methods, respectively. To investigate the surface composition of the catalyst, X-ray photoelectron spectroscopy (XPS) characterization was performed on a VG ESCALAB 220i-XL instrument with a monochromatic AlK $\alpha$  X-ray source.

## 2.3. Electrochemical Measurements

The catalytic activity was investigated by means of electrochemical methods conducted on an electrochemical work station (CHI 760E, Chenhua, Shanghai) in a three-electrode system. To prepare the working electrode: the catalyst (2.5 mg) was dispersed in ethanol (450  $\mu\text{L}$ ) and Nafion solution (50  $\mu\text{L}$ ) and treated ultrasonically for 30 min to obtain a homogeneous catalyst ink. Subsequently, the catalyst ink (10  $\mu\text{L}$ ) was added onto the GC electrode, yielding a working electrode with a catalyst loading of 0.25  $\text{mg cm}^{-2}$ . For comparison, a working electrode with Pt/C (20 Wt.% Pt) was also prepared and tested. A platinum wire and Hg/HgO were used as the counter and reference electrodes, respectively. The potentials were calibrated to a reversible hydrogen electrode ( $V_{\text{RHE}}$ ). Cyclic voltammetry (CV) and linear sweep voltammetry (LSV) techniques were applied for the catalytic performance investigation in the electrolyte of 0.1 M KOH saturated with  $\text{N}_2$  or  $\text{O}_2$ . The CVs obtained in the  $\text{N}_2$  saturated electrolyte at various scanning rate were used to evaluate the electrochemical active surface area (ECSA). The rotating ring disk electrode (RRDE) tests were conducted at a rate of 10  $\text{mV s}^{-1}$  with a ring potential of 1.5  $V_{\text{RHE}}$ . The catalyst stability was studied with a chronoamperometric current–time ( $i$ - $t$ ) curve at  $-0.2 \text{ V}$  (vs. Hg/HgO) in the  $\text{O}_2$ -saturated electrolyte with a rotation speed of 400 rpm.

Electrochemical impedance spectroscopy (EIS) was measured in the frequency range of 0.01 to 1,000,000 Hz at 0.7  $V_{\text{RHE}}$  with an amplitude of 0.005 V.

## 3. Results and Discussion

Figure 1 schematically shows the preparation process. The  $\text{NH}_4\text{HCO}_3$  decomposes at  $\sim 60^\circ\text{C}$ , generating a great amount of gases such as  $\text{NH}_3$  and  $\text{CO}_2$ . The gases result in the fabrication of pores in solid precursor. As the temperature increases, the sugar will melt to form a viscous sol, wrapping up the nitrate. As the temperature increases, the cobalt nitrate wrapped in the sol will decompose, and more porous structures will be fabricated by the

gases generated by the decomposition of the nitrate, resulting in a foam-like porous carbon being obtained. At the same time, N from the melamine can be doped into the carbon. As a result, Co-carrying N-doped carbon is obtained.

The SEM image (Figure 2a) shows that the Co/N-C-900 is randomly scattered as irregular particles with various sizes. Figure 2b shows the SEM image at higher magnification. Channels connecting the particles can be observed. Figure 2c is the SEM image at an even higher magnification, and pores can be observed in some particles. To demonstrate the pores more clearly, an enlarged image of the circled area in Figure 2c is presented in Figure 2d.

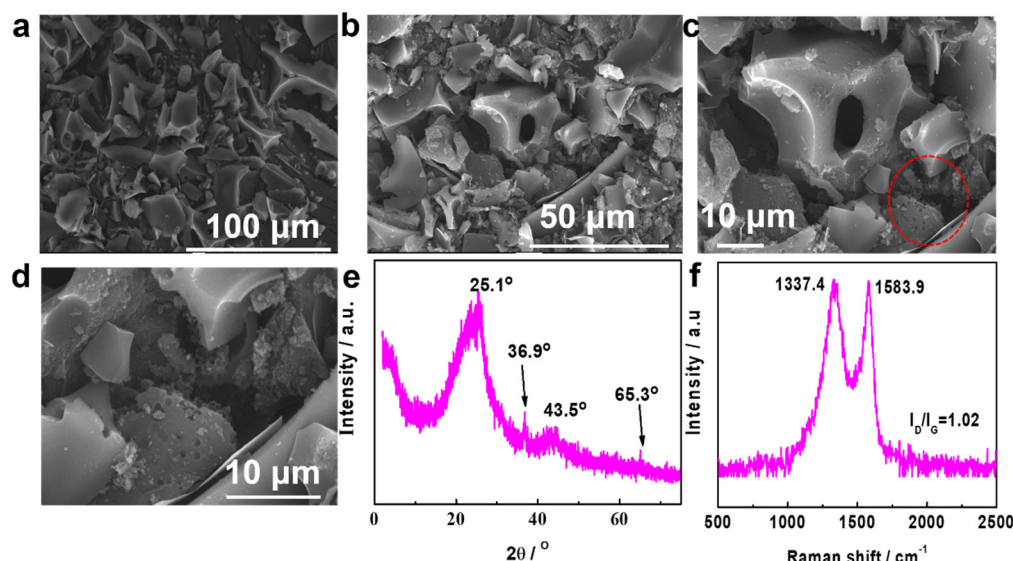


**Figure 2.** (a–d) SEM images at various magnifications for Co/N-C-900 (d presents enlarged image of the part in the red circle of c), (e) XRD pattern, (f) Raman spectra.

The crystallography of the Co/N-C-900 was studied using XRD (Figure 2e). The peaks at around 25.1 and 43.5° are related to the graphite (002, ICDD#41-1487) and (100) planes, respectively [21]. The two peaks indicate the formation of the graphite phase. The broad XRD peaks imply that crystallization is relatively low [22], and this is supported by the HRTEM images (Figure 3b). The peaks at 36.9 and 65.3° (ICDD # 00-042-1467) can be attributed to  $\text{Co}_3\text{O}_4$  [23], implying that Co has been doped into the carbon matrix. Figure 2f shows the Raman spectra for Co/N-C-900. Two peaks appear at 1337.4 and 1583.9  $\text{cm}^{-1}$  for the D and G bands, respectively. The peak for the D band is related to the disordered structure, implying that the graphite was successful doped with heteroatoms [24]. The G band peak is related to the  $\text{sp}^2$  hybridized carbon atoms [25]. The  $I_D/I_G$  for Co/N-C-900 is 1.02. This value is close to or higher than those of many other catalysts [26]. The high  $I_D/I_G$  suggests the richness of defective domains. This demonstrates that the Pharaoh's Snakes reaction is effective for fabricating the defective domains of the carbon material, and the defective domains are beneficial to catalytic performance [27].

The microstructure of the Co/N-C-900 was investigated further using TEM (Figure 3). Figure 3a confirms the structure of the channel-connected particles of the Co/N-C-900, which is in good agreement with the morphology, as shown in the SEM images (Figure 2). The channels and pores of the catalyst facilitate the transport of the reacting species to the active sites, which is helpful for improving catalytic performance. As shown in the HRTEM image (Figure 3b), a crystal lattice of 0.21 nm can be observed for graphite [28]. However, the crystal lattice is not continuous, implying that the carbon is amorphous. This is supported by the XRD pattern (Figure 2e), which has broad peaks. A crystal lattice spacing of 0.46 nm can also be observed. This lattice spacing is attributed to the  $\text{Co}_3\text{O}_4$  (111) plane [29], implying the existence of the  $\text{Co}_3\text{O}_4$ . The elemental distribution

of Co/N-C-900 was analyzed using energy dispersive spectroscopy (EDS) with scanning transmission electron microscopy (STEM). As shown in the STEM images in Figure 3c–f, the nitrogen (green) is distributed uniformly on the carbon (red), suggesting the efficient doping of the N into the carbon matrix. Figure 2f shows that there are Co species carried on the carbon. However, the Co distribution is not uniform. During the preparation, sugar powder,  $\text{NH}_4\text{HCO}_3$  and  $\text{Co}(\text{NO}_3)_2 \cdot 6\text{H}_2\text{O}$  can dissolved in the water. Therefore, the  $\text{Co}(\text{NO}_3)_2 \cdot 6\text{H}_2\text{O}$  can be distributed uniformly on the carbon source of the sugar. However, the melamine cannot be dissolved in water. As a result, the  $\text{Co}(\text{NO}_3)_2 \cdot 6\text{H}_2\text{O}$  cannot be distributed uniformly on the carbon and nitrogen source of the melamine. Therefore, the Co is not uniformly distributed on the carbon from the melamine. A longer grounding time for the solid precursor can improve the distribution, as shown in Figure S2.

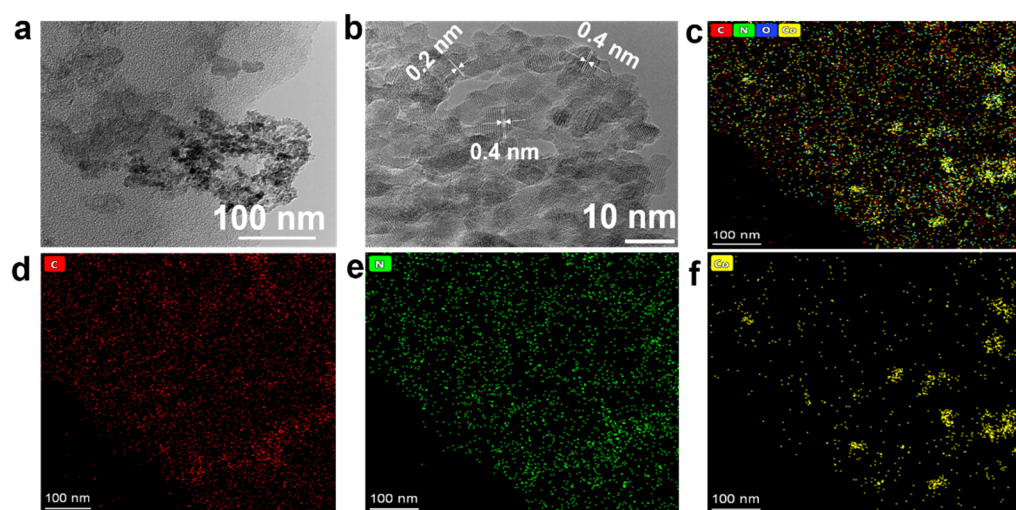


**Figure 3.** (a) TEM image of Co/N-C-900, (b) HRTEM image of Co/N-C-900, (c) EDS merged mapping image of C, N and Co, (d–f) EDS mapping images for C, N and Co, respectively.

The surface area as well as the pore width of the Co/N-C-900 were studied using the  $\text{N}_2$  adsorption/desorption isotherm. A type IV isotherm is displayed in Figure 4a, suggesting a mesoporous structure, and this is backed by the distribution curve of the pore size (Figure 4b), demonstrating that the pore size is mainly 3.8 nm. The Brunauer–Emmett–Teller (BET) surface area of the Co/N-C-900 is  $457.2 \text{ m}^2 \text{ g}^{-1}$ . The carbonized sugar surface area was increased as a result of the gas generated via the decomposition of the nitrate and the bicarbonate in the mixture. X-ray photoelectron spectroscopy (XPS, Figure 4c–f) was applied to study the surface composition of Co/N-C-900. XPS detected the carbon, nitrogen and cobalt content of 81.75, 5.58 and 1.36 at %, respectively, on the surface of Co/N-C-900. The C1s high-resolution spectrum (Figure 4d) can be deconvoluted into carboxyl (289.8 eV) [30], C-N=C (286.0 eV), C-N (284.9 eV), and C=C (284.3 eV) [31–33], implying that the N has been successfully doped into the carbon matrix. The N is more electrically negative than carbon, resulting in a re-distribution of the charge of the neighboring carbon, which changes the  $\text{O}_2$  chemisorption mode, weakening the O–O bonding and facilitating the ORR process [34]. Nitrogen doping also introduces spin density asymmetry, making it possible for the N-doped carbon to show electroncatalytic activities toward the ORR [35].

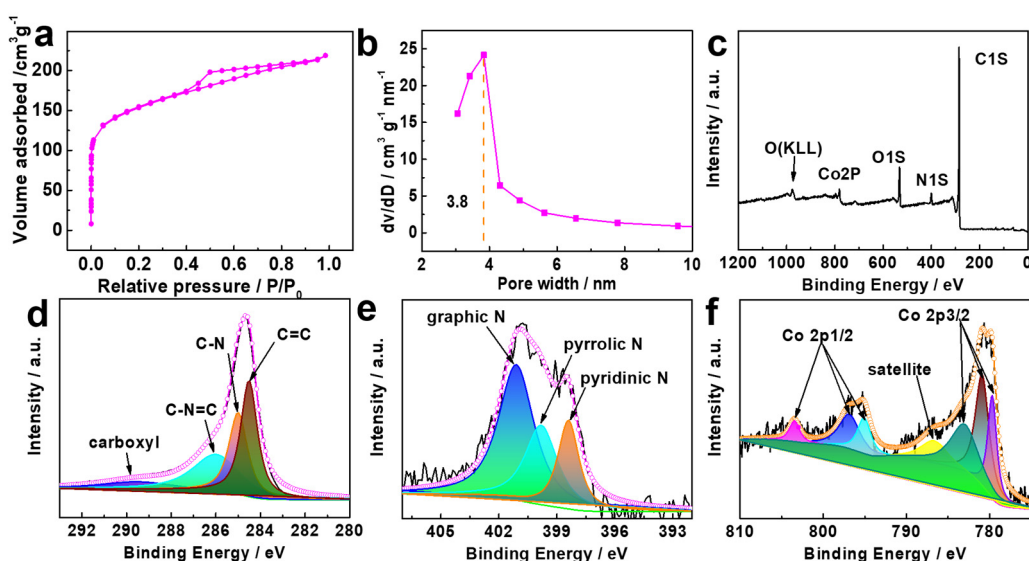


**Figure 4.** (a) Nitrogen sorption/desorption isotherm of the Co/N-C-900, (b) the corresponding pore width distribution curve, (c) XPS spectra survey of Co/N-C-900, (d) C1s XPS spectra, (e) N1s XPS spectra, (f) Co2p XPS spectra.

Figure 4e shows the high-resolution N1s spectra of Co/N-C-900, which can be deconvoluted into three peaks of pyridinic N (398.8 eV) [36], pyrrolic N (399.8 eV), and graphitic N(401.2 eV) [37]. Both the pyridinic N (20.1 at %) and the pyrrolic N (27.8 at %) have been considered to contribute ORR active sites [38,39]. Graphitic nitrogen is believed to be able to facilitate the electron transfer to the antibonding orbitals of oxygen from the carbon electronic bands [40,41]. The high-resolution Co spectrum (Figure 4f) can be resolved into Co 2p<sub>3/2</sub> and Co 2p<sub>1/2</sub> of Co<sup>2+</sup>/<sup>3+</sup>. The peaks at 780.94, 795.04 [42], 796.9 [43], and 805.5 eV [44] can be attributed to Co<sup>2+</sup>. The peaks at 779.74 [45], 780.94, and 786.73 eV can be attributed to Co2p<sub>3/2</sub> and the related satellite peaks [46]. The peak at 781.8 eV can be attributed to Co-N [47]. According to previous investigations [1], the M-N<sub>x</sub> (M: metal) and N-C moieties are both supposed to be active sites for ORR.

The catalytic performance was characterized using electrochemical methods. The CV tests were conducted first to evaluate the electrochemical activity. In the N<sub>2</sub>-saturated electrolyte, a featureless CV curve (Figure 5a) without peaks can be observed. However, a reduction peak can be observed in the O<sub>2</sub>-saturated electrolyte. These results suggest a facile ORR process on the Co/N-C-900. Subsequently, the catalytic activity on Co/N-C-900 toward ORR was characterized using rotating disk electrode (RDE) technology, and the LSVs are displayed in Figure 5b. The LSVs show an onset potential of 0.98 V<sub>RHE</sub>. This value is close to or higher than many reported values, such as (~0.74 V<sub>RHE</sub>) [48], as well as with respect to those reported for biomass such as typha orientalis (~0.87 V<sub>RHE</sub>) [49], eichhornia crassipes (~0.98 V<sub>RHE</sub>) [50], hair (~0.96 V<sub>RHE</sub>) [51], polyaniline with phytic acid (~0.94 V<sub>RHE</sub>) [26], and coconut shells (~0.87 V<sub>RHE</sub>) [52]. The half-wave potential of the Co/N-C-900 is 0.79 V<sub>RHE</sub>. The catalytic performance of commercial Pt/C was also investigated, and the LSV curve is presented in Figure 5b for comparison. The Co/N-C-900 demonstrated a catalytic activity close to that of the commercial Pt/C (20. Wt%), the onset and half-wave potentials of which were 0.98 and 0.81 V<sub>RHE</sub>, respectively. The limit current density of the Co/N-C-900 is 5.73 mA cm<sup>-2</sup>, which is almost same as that of the commercial Pt/C (20. Wt%), of 5.74 mA cm<sup>-2</sup>. Therefore, the “Pharaoh’s snakes” reaction holds great promise as a method for the preparation of Co, N co-doped NPMC toward the ORR.

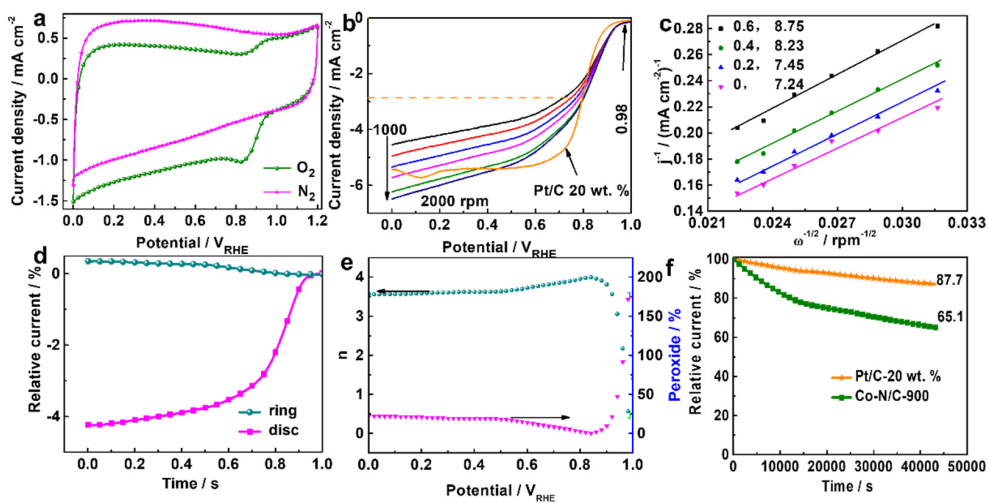


**Figure 5.** (a) CV on Co/N-C-900 in N<sub>2</sub>, O<sub>2</sub>-saturated electrolyte of 0.1M KOH solution, (b) LSV for Co/N-C-900 and Pt/C at 1600 rpm, (c) K-L lines. (d) LSV of the RRDE measurements (1600 rpm) of Co/N-C-900 (e) n and H<sub>2</sub>O<sub>2</sub>% at different potentials, (f) current–time curve 0.755 V<sub>RHE</sub> of Co/N-C-900 for ORR.

An increase in the current density, as shown in Figure 5b, can be observed with increasing rotational rate, resulting in higher oxygen flux to the electrode. The K-L lines (Koutecky–Levich lines, Figure 5c) were plotted as the inverse current density ( $j^{-1}$ ) vs. the inverse of the rotation speed square root ( $\omega^{1/2}$ ) at various electrode potentials. Based on the K-L lines, the apparent number of electrons transferred ( $n$ ) was investigated with the help of the K-L line slope at various potentials. The  $n$  was then calculated using Equations (1) and (2), in which  $j_k$  and  $j$  are the kinetic and measured current density, respectively,  $B$  is the reciprocal K-L line slope (found in the range of 7.24~8.75), as shown in Figure 5c,  $F$  is the Faraday constant (96,485 C mol<sup>-1</sup>),  $C_0$  is the bulk O<sub>2</sub> concentration ( $1.1 \times 10^{-3}$  mol L<sup>-3</sup>),  $D_0$  is the O<sub>2</sub> diffusion coefficient in 0.1 M KOH ( $1.9 \times 10^{-5}$  cm<sup>2</sup> s<sup>-1</sup>), and  $\gamma$  is the electrolyte kinetic viscosity (0.01 cm<sup>2</sup> s<sup>-1</sup>). The constant adopted when rpm is used to express the rotational rate was taken as 0.2 [53].

$$\frac{1}{j} = \frac{1}{j_k} + \frac{1}{B\omega^{1/2}} \quad (1)$$

$$B = 0.2nFC_O D_O^{2/3} \gamma^{-1/6} \quad (2)$$

The  $n$  varies slightly from 3.24 to 3.88, falling within the range 3.2~4.1 for the four-electron ORR pathway [54,55]. Therefore, the ORR on the Co/N-C-900 is largely a four-electron process. The linearity of the K-L line and the  $n$  value indicate the rapid kinetics with a predominant four-electron pathway in the investigated potential range. The four-electron ORR pathway is preferred in fuel cells and MABs for its high electron efficiency and low H<sub>2</sub>O<sub>2</sub> generation.

RRDE technology as applied to further evaluate the pathways for the ORR on the Co/N-C-900. As shown in Figure 5d, a low ring current density ( $\sim 0.25$  mA cm<sup>-2</sup>) for peroxide oxidation and high disk current density ( $\sim 4.2$  mA cm<sup>-2</sup>) for O<sub>2</sub> reduction can be observed, implying a small amount of H<sub>2</sub>O<sub>2</sub> generation and high catalytic performance toward ORR [56]. The  $n$  and HO<sub>2</sub><sup>-</sup>% were calculated according to Equations (3) and (4), respectively [57].

$$n = 4 \frac{i_d}{i_d + i_{r/N}} \quad (3)$$

$$\text{HO}_2^- \% = 200 \frac{\frac{i_r}{N}}{i_d + i_{r/N}} \quad (4)$$

where  $i_d$  and  $i_r$  are the ring and disk current, respectively.  $N$  is the current collection efficiency of the Pt ring, and was determined to be 0.39. The  $n$  and  $\text{HO}_2^- \%$  at various potentials are shown in Figure 5e. The average  $n$  is higher than 3.5 in the potential range of 0~0.9 V<sub>RHE</sub>, indicating the mainly four-electron pathway ORR pathway, which is in good agreement with the results from the RDE. The  $\text{HO}_2^- \%$  is lower than 25% in the range of 0 to 0.9 V<sub>RHE</sub>. The  $\text{HO}_2^-$  generation is close to the values reported for other materials, such as 24.6% [12] and ~20% [56]. Therefore, Co/N-C-900 is a promising ORR NPMC for fuel cells and MABs.

The ORR stability of Co/N-C-900 was investigated via chronoamperometry at 0.755 V<sub>RHE</sub> in an O<sub>2</sub>-saturated electrolyte of 0.1 M KOH solution. The current–time curve for Co/N-C-900 in Figure 5g remains at around 90% and at around 65% of the initial current value after stability tests of 3600 s and 432,000 s, respectively. The stability is still lower than that of the commercial Pt/C, as shown in Figure 5f, which shows a stability of 87.7% after the 42,000 s stability test. The Tafel plots (Figure S3 in the ESI) for Co/N-C-900 and Pt/C were investigated in the corresponding potential range between the onset and half-wave potentials. The Tafel slope of Co/N-C-900 was 136.9 mV dec<sup>-1</sup>, which is higher than that obtained for Pt/C. The higher Tafel slope implies a faster overpotential increase with current density [58]. The stability and Tafel mean that the Co/N-C-900 possesses lower catalytic activity than the commercial Pt/C. However, the lower price of Co/N-C-900 still makes it a promising candidate as an ORR catalyst.

The effect of the pyrolyzing temperature on the catalytic activity was investigated. Figure 6a shows the LSV for the ORR occurring on the catalysts obtained using pyrolyzing temperatures of 800, 900 and 1000 °C. The catalyst prepared with a temperature of 900 °C showed the highest catalytic performance. The results imply that 900 °C is the optimal pyrolyzing temperature. Usually, a high pyrolyzing temperature is favorable for the carbonization of the catalyst [59] and helpful for improving the conductivity and electrocatalytic performance. However, high temperatures can cause a decrease in the number of heteroatoms [59], resulting in a reduction in catalytic performance. Therefore, there is usually an optimal pyrolyzing temperature for catalysts prepared via the pyrolyzation process, similar to what has been reported in other work [60].

CV tests were carried out at different scanning rates to measure the ECSA. The CV curves for the Co/N-C-800, 900 and 1000 are displayed in Figure S4 in the ESI. The lines in Figure 6b were determined by plotting the CV curve for the closed area vs. the scanning rate. The ECSA can be evaluated using line slopes proportional to the corresponding ECSAs [61]. The slope for Co/N-C-900 was higher than those of Co/N-C-800 and Co/N-C-1000. Therefore, the Co/N-C-900 possessed the highest ECSA. To further investigate the mechanism for the differences in catalytic performance among the Co/N-C-800, 900 and 1000, EIS measurements were conducted for the three samples, and the EIS plots are presented in Figure 6c. An enlarged figure is presented in Figure 6d showing the EIS plots for high frequencies more clearly. The EIS plots in Figure 6c,d indicate that the conductivity of Co/N-C-900 was higher than those of Co/N-C-900 and Co/N-C-1000. The high values of ECSA and conductivity may also be reasons explaining the high catalytic activity of Co/N-C-900.

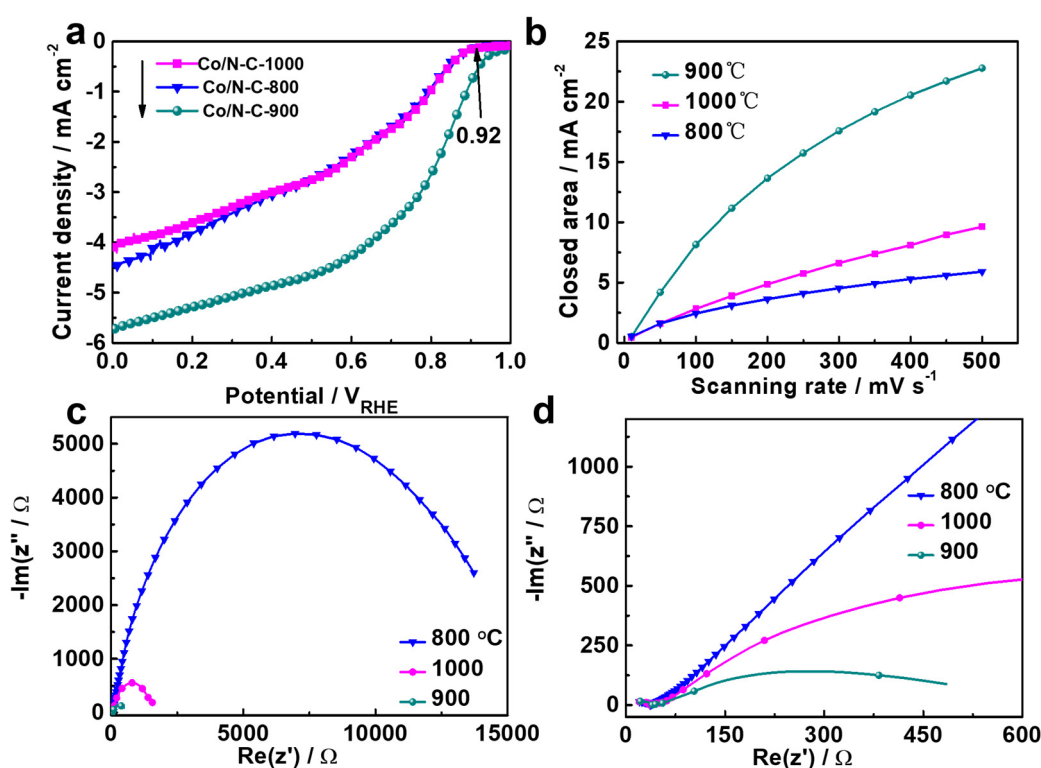


**Figure 6.** (a) LSV for the Co/N-C prepared at various temperatures, (b) CV closed area vs. scanning rate, (c) EIS, (d) enlarged EIS of the high-frequency part.

#### 4. Conclusions

The ancient chemical magic “Pharaoh’s snakes” reaction was used to prepare  $\text{Co}_3\text{O}_4$  carrying N-doped porous carbon (Co/N-C) as a non-precious metal catalyst for ORR, an important electrode reaction in fuel cells and metal–air batteries. The “Pharaoh’s snakes” reaction possesses the advantages of being low cost, facile, and fast in the preparation of Co/N-C catalyst for ORR. The obtained catalyst showed considerable activity towards ORR, with an onset potential of 0.98 V<sub>RHE</sub> and a half-wave potential of 0.79 V<sub>RHE</sub> in 0.1 M KOH solution as electrolyte. This investigation provides a promising alternative method for the preparation of Co, N co-doped non-precious-metal catalyst for ORR, an important electrode reaction for fuel cells and metal–air batteries such as Zn–air and Li–air batteries.

**Supplementary Materials:** The following supporting information can be downloaded at: <https://www.mdpi.com/article/10.3390/batteries8100150/s1>; Figure S1: Temperature-time curve; Figure S2: SEM mapping, (a) SEM image, (b) C, (c) N, (d) Co; Figure S3: Tafel plots of Co/N-C-900 and Pt/C 20 wt. %; Figure S4: CV curves at various scanning rates for Co/N-C-800(a), Co/N-C-900(b) and Co/N-C-1000 (c).

**Author Contributions:** Conceptualization, J.G. and Z.Y.; methodology, H.W.; validation, X.T.; formal analysis, Y.L.; investigation, M.Z., X.W. All authors have read and agreed to the published version of the manuscript.

**Funding:** This research received no external funding.

**Data Availability Statement:** Not applicable.

**Acknowledgments:** This work was supported by National Natural Science Foundation of China (No. 21776219, 21872104) and Tianjin Key Laboratory of Green Chemical Engineering Process Engineering, Tiangong University, GCEPE20190106. Jian Gao appreciate the support of from China Postdoctoral Science Foundation (No. 2018M631746) and Basic Research Program of Jiangsu (SBK20201213).

**Conflicts of Interest:** The authors declare no conflict of interest.

## References

- Wang, D.; Pan, X.; Yang, P.; Li, R.; Xu, H.; Li, Y.; Meng, F.; Zhang, J.; An, M. Transition metal and nitrogen Co-doped carbon-based electrocatalysts for the oxygen reduction reaction: From active site insights to the rational design of precursors and structures. *ChemSusChem* **2021**, *14*, 33–55. [[CrossRef](#)] [[PubMed](#)]
- Li, G.; Wang, X.L.; Fu, J.; Li, J.D.; Park, M.G.; Zhang, Y.N.; Lui, G.; Chen, Z.W. Pomegranate-inspired design of highly active and durable bifunctional electrocatalysts for rechargeable metal-air batteries. *Angew. Chem. Int. Ed.* **2016**, *55*, 4977–4982. [[CrossRef](#)] [[PubMed](#)]
- Liu, Z.; Zhao, Z.; Peng, B.; Duan, X.; Huang, Y. Beyond extended surfaces: Understanding the oxygen reduction reaction on nanocatalysts. *J. Am. Chem. Soc.* **2020**, *142*, 17812–17827. [[CrossRef](#)] [[PubMed](#)]
- Li, J.; Hou, L.; Yu, M.; Li, Q.; Zhang, T.; Sun, H. Review and recent advances of oxygen transfer in Li-air batteries. *ChemElectroChem* **2021**, *8*, 3588–3603. [[CrossRef](#)]
- Liu, B.; Sun, Y.; Liu, L.; Xu, S.; Yan, X. Advances in manganese-mased oxides cathodic electrocatalysts for Li–Air batteries. *Adv. Funct. Mater.* **2018**, *28*, 1704973. [[CrossRef](#)]
- Xiao, Y.; Wang, J.; Wang, Y.; Zhang, W. A new promising catalytic activity on blue phosphorene nitrogen-doped nanosheets for the ORR as cathode in nonaqueous Li-air batteries. *Appl. Surf. Sci.* **2019**, *488*, 620–628. [[CrossRef](#)]
- Wroblowa, H.S.; Razumney, G. Electroreduction of oxygen: A new mechanistic criterion. *J. Electroanal. Chem. Interfacial Electrochem.* **1976**, *69*, 195–201. [[CrossRef](#)]
- Luo, E.; Chu, Y.; Liu, J.; Shi, Z.; Zhu, S.; Gong, L.; Ge, J.; Choi, C.H.; Liu, C.; Xing, W. Pyrolyzed M–N x catalysts for oxygen reduction reaction: Progress and prospects. *Energy Environ. Sci.* **2021**, *14*, 2158–2185. [[CrossRef](#)]
- Chen, Z.W.; Higgins, D.; Yu, A.P.; Zhang, L.; Zhang, J.J. A review on non-precious metal electrocatalysts for PEM fuel cells. *Energy Environ. Sci.* **2011**, *4*, 3167–3192. [[CrossRef](#)]
- Sun, Z.; Yuan, M.; Lin, L.; Yang, H.; Nan, C.; Sun, G.; Li, H.; Yang, X. Perovskite La<sub>0.5</sub>Sr<sub>0.5</sub>CoO<sub>3–δ</sub> grown on Ti<sub>3</sub>C<sub>2</sub>T x MXene nanosheets as bifunctional efficient hybrid catalysts for Li–Oxygen batteries. *ACS Appl. Energy Mater.* **2019**, *2*, 4144–4150. [[CrossRef](#)]
- Clark, S.; Latz, A.; Horstmann, B. A review of model-based design tools for metal-air batteries. *Batteries* **2018**, *4*, 5. [[CrossRef](#)]
- Ren, G.Y.; Gao, L.L.; Teng, C.; Li, Y.A.; Yang, H.Q.; Shui, J.L.; Lu, X.Y.; Zhu, Y.; Dai, L.M. Ancient chemistry "Pharaoh's Snakes" for efficient Fe-/N-doped carbon electrocatalysts. *ACS Appl. Mater. Interfaces* **2018**, *10*, 10778–10785. [[CrossRef](#)] [[PubMed](#)]
- Zion, N.; Cullen, D.A.; Zelenay, P.; Elbaz, L. Heat-treated aerogel as a catalyst for the oxygen reduction reaction. *Angew. Chem. Int. Ed.* **2020**, *132*, 2504–2510. [[CrossRef](#)]
- Yang, L.; Zeng, X.; Wang, W.; Cao, D. Recent progress in MOF-derived, heteroatom-doped porous carbons as highly efficient electrocatalysts for oxygen reduction reaction in fuel cells. *Adv. Funct. Mater.* **2018**, *28*, 1704537. [[CrossRef](#)]
- Liang, H.-W.; Zhuang, X.; Brüller, S.; Feng, X.; Müllen, K. Hierarchically porous carbons with optimized nitrogen doping as highly active electrocatalysts for oxygen reduction. *Nat. Commun.* **2014**, *5*, 4973. [[CrossRef](#)]
- Ingo, G.M.; Guida, G.; Angelini, E.; Di Carlo, G.; Mezzi, A.; Padeletti, G. Ancient mercury-based plating methods: Combined use of surface analytical techniques for the study of manufacturing process and degradation phenomena. *Acc. Chem. Res.* **2013**, *46*, 2365–2375. [[CrossRef](#)]
- Buelens, L.C.; Galvita, V.V.; Poelman, H.; Detavernier, C.; Marin, G.B. Super-dry reforming of methane intensifies CO<sub>2</sub> utilization via Le Chatelier's principle. *Science* **2016**, *354*, 449–452. [[CrossRef](#)]
- Xie, X.H.; He, C.; Li, B.Y.; He, Y.H.; Cullen, D.A.; Wegener, E.C.; Kropf, A.J.; Martinez, U.; Cheng, Y.W.; Engelhard, M.H.; et al. Performance enhancement and degradation mechanism identification of a single-atom Co-N-C catalyst for proton exchange membrane fuel cells. *Nat. Catal.* **2020**, *3*, 1044–1054. [[CrossRef](#)]
- Wang, X.X.; Prabhakaran, V.; He, Y.; Shao, Y.; Wu, G. Iron-free cathode catalysts for proton-exchange-membrane fuel cells: Cobalt catalysts and the peroxide mitigation approach. *Adv. Mater.* **2019**, *31*, 1805126. [[CrossRef](#)]
- Wang, J.; Gao, R.; Zhou, D.; Chen, Z.; Wu, Z.; Schumacher, G.; Hu, Z.; Liu, X. Boosting the electrocatalytic activity of Co<sub>3</sub>O<sub>4</sub> nanosheets for a Li–O<sub>2</sub> battery through modulating inner oxygen vacancy and exterior Co<sup>3+</sup>/Co<sup>2+</sup> ratio. *ACS Catal.* **2017**, *7*, 6533–6541. [[CrossRef](#)]
- Gao, J.; Wang, Y.; Wu, H.; Liu, X.; Wang, L.; Yu, Q.; Li, A.; Wang, H.; Song, C.; Gao, Z.; et al. Construction of a sp<sup>3</sup>/sp<sup>2</sup> carbon interface in 3D N-doped nanocarbons for the oxygen reduction reaction. *Angew. Chem. Int. Ed.* **2019**, *58*, 15089–15097. [[CrossRef](#)]
- Chen, J.; Wang, X.; Cui, X.; Yang, G.; Zheng, W. Amorphous carbon enriched with pyridinic nitrogen as an efficient metal-free electrocatalyst for oxygen reduction reaction. *Chem. Commun.* **2014**, *50*, 557–559. [[CrossRef](#)] [[PubMed](#)]
- Gao, J.; Ma, N.; Zheng, Y.; Zhang, J.; Gui, J.; Guo, C.; An, H.; Tan, X.; Yin, Z.; Ma, D. Cobalt/nitrogen-doped porous carbon nanosheets derived from polymerizable ionic liquids as bifunctional electrocatalyst for oxygen evolution and oxygen reduction reaction. *ChemCatChem* **2017**, *9*, 1601–1609. [[CrossRef](#)]
- Wei, D.C.; Liu, Y.Q.; Wang, Y.; Zhang, H.L.; Huang, L.P.; Yu, G. Synthesis of N-doped graphene by chemical vapor deposition and its electrical properties. *Nano Lett.* **2009**, *9*, 1752–1758. [[CrossRef](#)] [[PubMed](#)]
- Wang, J.; Gao, D.; Wang, G.; Miao, S.; Wu, H.; Li, J.; Bao, X. Cobalt nanoparticles encapsulated in nitrogen-doped carbon as a bifunctional catalyst for water electrolysis. *J. Mater. Chem. A* **2014**, *2*, 20067–20074. [[CrossRef](#)]
- Zhang, J.; Zhao, Z.; Xia, Z.; Dai, L. A metal-free bifunctional electrocatalyst for oxygen reduction and oxygen evolution reactions. *Nat. Nanotechnol.* **2015**, *10*, 444–452. [[CrossRef](#)] [[PubMed](#)]

27. Yan, X.; Jia, Y.; Odedairo, T.; Zhao, X.; Jin, Z.; Zhu, Z.; Yao, X. Activated carbon becomes active for oxygen reduction and hydrogen evolution reactions. *Chem. Commun.* **2016**, *52*, 8156–8159. [CrossRef] [PubMed]
28. Li, M.; Hu, C.; Yu, C.; Wang, S.; Zhang, P.; Qiu, J. Organic amine-grafted carbon quantum dots with tailored surface and enhanced photoluminescence properties. *Carbon* **2015**, *91*, 291–297. [CrossRef]
29. Hemamalini, S.; Manimekalai, R. Synthesis, structural, magnetic, textural, optical investigation and photocatalytic performance of undoped and doped cobaltite nanoparticles. *J. Coord. Chem.* **2020**, *73*, 3431–3451. [CrossRef]
30. Osbeck, S.; Bradley, R.; Liu, C.; Idriss, H.; Ward, S. Effect of an ultraviolet/ozone treatment on the surface texture and functional groups on polyacrylonitrile carbon fibres. *Carbon* **2011**, *49*, 4322–4330. [CrossRef]
31. Chao, H.; Chang, Y.; Mingyu, L.; Xiuna, W.; Qiang, D.; Gang, W.; Jieshan, Q. Nitrogen-doped carbon dots decorated on graphene: A novel all-carbon hybrid electrocatalyst for enhanced oxygen reduction reaction. *Chem. Commun.* **2015**, *51*, 3419–3422.
32. Tahir, M.; Mahmood, N.; Zhang, X.X.; Mahmood, T.; Butt, F.K.; Aslam, I.; Tanveer, M.; Idrees, F.; Khalid, S.; Shakir, I.; et al. Bifunctional catalysts of  $\text{Co}_3\text{O}_4@\text{GCN}$  tubular nanostructured (TNS) hybrids for oxygen and hydrogen evolution reactions. *Nano Res.* **2015**, *8*, 3725–3736. [CrossRef]
33. Zhou, G.-W.; Wang, J.; Gao, P.; Yang, X.; He, Y.-S.; Liao, X.-Z.; Yang, J.; Ma, Z.-F. Facile spray drying route for the three-dimensional graphene-encapsulated  $\text{Fe}_2\text{O}_3$  nanoparticles for lithium ion battery anodes. *Ind. Eng. Chem. Res.* **2013**, *52*, 1197–1204. [CrossRef]
34. Gong, K.; Du, F.; Xia, Z.; Durstock, M.; Dai, L. Nitrogen-doped carbon nanotube arrays with high electrocatalytic activity for oxygen reduction. *Science* **2009**, *323*, 760–764. [CrossRef] [PubMed]
35. Zhang, L.; Xia, Z. Mechanisms of Oxygen Reduction Reaction on Nitrogen-Doped Graphene for Fuel Cells. *J. Phys. Chem. C* **2011**, *115*, 11170–11176. [CrossRef]
36. Kurak, K.A.; Anderson, A.B. Nitrogen-treated graphite and oxygen electroreduction on pyridinic edge sites. *J. Phys. Chem. C* **2009**, *113*, 6730–6734. [CrossRef]
37. Xiang, Z.; Xue, Y.; Cao, D.; Huang, L.; Chen, J.F.; Dai, L. Highly efficient electrocatalysts for oxygen reduction based on 2D covalent organic polymers complexed with non-precious metals. *Angew. Chem. Int. Ed.* **2014**, *53*, 2433–2437. [CrossRef] [PubMed]
38. Cui, X.; Yang, S.; Yan, X.; Leng, J.; Shuang, S.; Ajayan, P.M.; Zhang, Z. Pyridinic-nitrogen-Dominated graphene aerogels with Fe–N–C coordination for highly efficient oxygen reduction reaction. *Adv. Funct. Mater.* **2016**, *26*, 5708–5717. [CrossRef]
39. Kang, G.-S.; Jang, J.-H.; Son, S.-Y.; Lee, Y.-K.; Lee, D.C.; Yoo, S.J.; Lee, S.; Joh, H.-I. Pyrrolic N wrapping strategy to maximize the number of single-atomic Fe-Nx sites for oxygen reduction reaction. *J. Power Sources* **2022**, *520*, 230904. [CrossRef]
40. Zhu, J.; He, C.; Li, Y.; Kang, S.; Shen, P.K. One-step synthesis of boron and nitrogen-dual-self-doped graphene sheets as non-metal catalysts for oxygen reduction reaction. *J. Mater. Chem. A* **2013**, *1*, 14700–14705. [CrossRef]
41. Wang, P.; Wang, Z.; Jia, L.; Xiao, Z. Origin of the catalytic activity of graphite nitride for the electrochemical reduction of oxygen: Geometric factors vs. electronic factors. *Phys. Chem. Chem. Phys.* **2009**, *11*, 2730–2740. [CrossRef] [PubMed]
42. Ma, T.; Zhang, M.; Liu, H.; Wang, Y. Three-dimensional sulfur-doped graphene supported cobalt-molybdenum bimetallic sulfides nanocrystal with highly interfacial storage capability for supercapacitor electrodes. *Electrochim. Acta* **2019**, *322*, 134762. [CrossRef]
43. Hong, Q.-L.; Zhai, Q.-G.; Liang, X.-L.; Yang, Y.; Li, F.-M.; Jiang, Y.-C.; Hu, M.-C.; Li, S.-N.; Chen, Y. Holey cobalt oxyhydroxide nanosheets for the oxygen evolution reaction. *J. Mater. Chem. A* **2021**, *9*, 3297–3302. [CrossRef]
44. Ren, X.; Ge, R.; Zhang, Y.; Liu, D.; Wu, D.; Sun, X.; Du, B.; Wei, Q. Cobalt–borate nanowire array as a high-performance catalyst for oxygen evolution reaction in near-neutral media. *J. Mater. Chem. A* **2017**, *5*, 7291–7294. [CrossRef]
45. Béjar, J.; Álvarez-Contreras, L.; Ledesma-García, J.; Arjona, N.; Arriaga, L.G. An advanced three-dimensionally ordered macroporous  $\text{NiCo}_2\text{O}_4$  spinel as a bifunctional electrocatalyst for rechargeable Zn-air batteries. *J. Mater. Chem. A* **2020**, *8*, 8554–8565. [CrossRef]
46. Liang, Z.; Dong, X. Co<sub>2</sub>P nanosheet cocatalyst-modified Cd<sub>0.5</sub>Zn<sub>0.5</sub>S nanoparticles as 2D-0D heterojunction photocatalysts toward high photocatalytic activity. *J. Photochem. Photobiol. A Chem.* **2021**, *407*, 113081. [CrossRef]
47. Niu, K.; Yang, B.; Cui, J.; Jin, J.; Fu, X.; Zhao, Q.; Zhang, J. Graphene-based non-noble-metal Co/N/C catalyst for oxygen reduction reaction in alkaline solution. *J. Power Sources* **2013**, *243*, 65–71. [CrossRef]
48. Zhang, J.; Zhang, G.; Jin, S.; Zhou, Y.; Ji, Q.; Lan, H.; Liu, H.; Qu, J. Graphitic N in nitrogen-doped carbon promotes hydrogen peroxide synthesis from electrocatalytic oxygen reduction. *Carbon* **2020**, *163*, 154–161. [CrossRef]
49. Chen, P.; Wang, L.-K.; Wang, G.; Gao, M.-R.; Ge, J.; Yuan, W.-J.; Shen, Y.-H.; Xie, A.-J.; Yu, S.-H. Nitrogen-doped nanoporous carbon nanosheets derived from plant biomass: An efficient catalyst for oxygen reduction reaction. *Energy Environ. Sci.* **2014**, *7*, 4095–4103. [CrossRef]
50. Liu, X.; Zhou, Y.; Zhou, W.; Li, L.; Huang, S.; Chen, S. Biomass-derived nitrogen self-doped porous carbon as effective metal-free catalysts for oxygen reduction reaction. *Nanoscale* **2015**, *7*, 6136–6142. [CrossRef]
51. Chaudhari, K.N.; Song, M.Y.; Yu, J.S. Transforming hair into heteroatom-doped carbon with high surface area. *Small* **2014**, *10*, 2625–2636. [CrossRef] [PubMed]
52. Borghei, M.; Laocharoen, N.; Kibena-Pöldsepp, E.; Johansson, L.-S.; Campbell, J.; Kauppinen, E.; Tammeveski, K.; Rojas, O.J. Porous N, P-doped carbon from coconut shells with high electrocatalytic activity for oxygen reduction: Alternative to Pt-C for alkaline fuel cells. *Appl. Catal. B Environ.* **2017**, *204*, 394–402. [CrossRef]
53. Wang, S.; Yu, D.; Dai, L. Polyelectrolyte functionalized carbon nanotubes as efficient metal-free electrocatalysts for oxygen reduction. *J. Am. Chem. Soc.* **2011**, *133*, 5182–5185. [CrossRef]

54. Wang, Y.; Jiang, X. Facile preparation of porous carbon nanosheets without nematicle and their excellent electrocatalytic property. *ACS Appl. Mater. Interfaces* **2013**, *5*, 11597–11602. [[CrossRef](#)] [[PubMed](#)]
55. Yang, W.; Fellinger, T.-P.; Antonietti, M. Efficient metal-free oxygen reduction in alkaline medium on high-surface-area mesoporous nitrogen-doped carbons made from ionic liquids and nucleobases. *J. Am. Chem. Soc.* **2011**, *133*, 206–209. [[CrossRef](#)]
56. Chen, P.; Zang, J.; Zhou, S.; Jia, S.; Tian, P.; Cai, H.; Gao, H.; Wang, Y. N-doped 3D porous carbon catalyst derived from biowaste Triarrhena sacchariflora particle for oxygen reduction reaction. *Carbon* **2019**, *146*, 70–77. [[CrossRef](#)]
57. Wu, C.-H.; Wang, K.-C.; Chang, S.-T.; Chang, Y.-C.; Chen, H.-Y.; Yamanaka, I.; Chiang, T.-C.; Huang, H.-C.; Wang, C.-H. High performance of metal-organic framework-derived catalyst supported by tellurium nanowire for oxygen reduction reaction. *Renew. Energ.* **2020**, *158*, 324–331. [[CrossRef](#)]
58. Kim, S.; Myles, T.D.; Kunz, H.R.; Kwak, D.; Wang, Y.; Maric, R. The effect of binder content on the performance of a high temperature polymer electrolyte membrane fuel cell produced with reactive spray deposition technology. *Electrochim. Acta* **2015**, *177*, 190–200. [[CrossRef](#)]
59. Lin, L.; Zhu, Q.; Xu, A.-W. Noble-metal-free Fe-N/C catalyst for highly efficient oxygen reduction reaction under both alkaline and acidic conditions. *J. Am. Chem. Soc.* **2014**, *136*, 11027–11033. [[CrossRef](#)]
60. Li, S.; Zhang, L.; Liu, H.; Pan, M.; Zan, L.; Zhang, J. Heat-treated cobalt-triptyridyl triazine (Co-TPTZ) electrocatalysts for oxygen reduction reaction in acidic medium. *Electrochim. Acta* **2010**, *55*, 4403–4411. [[CrossRef](#)]
61. McCrory, C.C.L.; Jung, S.; Peters, J.C.; Jaramillo, T.F. Benchmarking heterogeneous electrocatalysts for the oxygen evolution reaction. *J. Am. Chem. Soc.* **2013**, *135*, 16977–16987. [[CrossRef](#)] [[PubMed](#)]